Processing and Application of Ceramics 13 [4] (2019) 333–341
https://doi.org/10.2298/PAC1904333V

BY-NC-ND

Effects of Sr and Mn co-doping on microstructural evolution and electrical properties of $LaAlO_3$

Lúcia Adriana Villas-Boas[1,*], Celso Antonio Goulart[2], Dulcina Pinatti Ferreira de Souza[2]

[1]*São Paulo State University (UNESP), School of Sciences and Engineering, Postal Code 17602-496, Tupã, SP, Brazil*

[2]*Graduate Program in Materials Science and Engineering, Department of Materials Engineering, Federal University of São Carlos, Postal Code 13565-905, São Carlos, SP, Brazil*

Received 23 March 2019; Received in revised form 3 July 2019; Accepted 20 September 2019

Abstract

In this work, we investigate the effects of Sr and Mn co-doping on the microstructural development and electrical properties of $LaAlO_3$ synthesised by solid state reaction and sintered at 1500 and 1600 °C. The addition of Sr and Mn contributed to the crystallization and stabilization of the perovskite structure. However, the addition of Sr alone lead to the formation of heterogeneous microstructure, while the combined effect of Sr and Mn improved Al and La homogeneity in the perovskite structure. Total electrical conductivity is enhanced by three orders of magnitude with Sr addition ($La_{0.8}Sr_{0.2}AlO_{3-\delta}$: 5.74×10^{-4} S/cm at 600 °C) and five orders of magnitude with Mn co-doping ($La_{0.8}Sr_{0.2}Al_{0.8}Mn_{0.2}O_{3-\delta}$: 3.6×10^{-2} S/cm at 600 °C) compared to the undoped $LaAlO_3$ (2.96×10^{-6} S/cm at 600 °C). The Sr and Mn co-doped $LaAlO_3$ present favourable catalytic activity for electrode reactions even with a low dopant concentration (20 mol%).

Keywords: *perovskite oxides, $LaAlO_3$, doping, electrical conduction*

I. Introduction

Perovskite-type and perovskite-related structures constitute an important class of materials and have received considerable attention for applications in physics, solid-state chemistry and advanced materials due to their outstanding properties. These materials present general formula ABX_3 and can accommodate a variety of elements in the crystal lattice without destroying the matrix structure, in which A positions are generally occupied by a rare earth metal or alkaline earth metal cation, B positions with small transition metal cations and X denotes oxygen anions. This structural diversity offers numerous advantages in terms of compounds with enhanced properties, such as thermal and chemical stability in large range of oxygen partial pressure, and ionic, protonic and electronic conductivity [1].

Mixed conducting perovskites are the most applied and studied materials and have been used as components in oxygen separation membranes, chemical sensors, oxygen pumps, thermoelectric devices, catalyst for combustion of hydrocarbons decomposition and application in solid oxide fuel cells (SOFC) as electrodes and electrolytes materials [2,3]. For any of these applications, the promising properties of perovskites are obtained by properly selecting their crystalline structure and symmetries. It is important to control stoichiometry and microstructure, avoiding secondary phases that can deteriorate any functional properties [4,5].

Among perovskite-type oxides, lanthanum aluminate ($LaAlO_3$) exhibit interesting electrical and electrocatalytic properties, with application in numerous fields, such as high frequency capacitors, substrate material for thin film high temperature superconductors, and electrolyte material for solid oxide fuel cells (SOFC) [1–3,6]. The properties of this material arise from substitution by different dopants either on the La or Al sites. Consequently, oxygen vacancies are generated to compensate the electrical charge of substituting ions. Since the electrical conductivity of $LaAlO_3$ is significantly affected by adding appropriate dopants, systems based on $LaAlO_3$ are known to be mixed ionic and p-type electronic conductors at high oxygen partial pressure and

*Corresponding author: tel: +55 1434044272,
e-mail: *lucia.villas-boas@unesp.br*

good ionic conductors at low oxygen partial pressure. These materials have also low cost, higher stability in different types of atmospheres, and moderate thermal expansion, which make them adequate for SOFC applications [7–11].

In the present study, we investigate the effects of Sr and Mn co-doping at A and B sites of $LaAlO_3$ on the microstructural development and electrical properties, using a concentration of 20 mol% of each dopant to create a reasonable number of oxygen vacancies and electronic holes.

II. Experimental

2.1. Sample preparation

Pure, Sr-doped and Sr and Mn co-doped $LaAlO_3$ powders were synthesized by solid-state reaction method, using La_2O_3 (Aldrich, 99.9%), Al_2O_3 (Baikowski-CR30), $Sr(NO_3)_2$ (Riedel-de Haën, 99.99%) and $Mn(NO_3)_2 \cdot 6H_2O$ (Aldrich, 99.9%). Suitable amounts of each raw material were mixed in isopropyl alcohol for 12 h in a vibratory mill with zirconia milling media ($\varnothing$ = 3 mm, YTZ Grinding Media Tosoh, Japan). The suspensions were dried at room temperature, after which the resulting powders were calcined at 800 °C in air for 30 min. This procedure was repeated twice. The calcined powders were then milled in vibratory mill with isopropyl alcohol and 1 wt.% of poly-vinylbutyral (B-98, Solutia). The suspensions were dried and deagglomerated through an 80 mesh nylon sieve. The powders were formed into pellets by uniaxial pressing (100 MPa) followed by and isostatic pressing (200 MPa) and sintered at 1500 and 1600 °C in air with a dwell time of 6 h. Table 1 lists their compositions and respective identifications.

Table 1. Sample identification

Composition	Sample identification
$LaAlO_3$	LA
$La_{0.8}Sr_{0.2}AlO_{3-\delta}$	LSA
$La_{0.8}Sr_{0.2}Al_{0.8}Mn_{0.2}O_{3-\delta}$	LSAM

2.2. Sample characterization

X-ray diffraction (XRD, Siemens D5000, Cu Kα radiation, 2θ = 15–80°, 0.02 °/s) was used to evaluate crystal structure of each powder. The cell parameters were determined by Rietveld refinement using the General Structure Analysis System (GSAS) software, using the graphical interface EXPGU and ICSD (Inorganic Crystal Structure Database) CIF files.

The bulk densities of sintered samples were determined by the Archimedes principle using an analytical balance (Metler Toledo AX 204). Relative density was derived using the theoretical value determined from the experimental lattice parameters and the measured one. The microstructure of polished and etched surfaces of sintered samples was analysed by scanning electron microscopy (SEM, Phillips XL 30 FEG). Grain size and grain size distribution were calculated by analysing SEM images (at least 100 grains for each sample) with the open license software ImageJ and then treating the data with the software Minitab®.

The pellets were characterized electrically by impedance spectroscopy (Impedance analyser HP 4192A LF) in the frequency range of 13 MHz to 5 Hz with AC current amplitude of 500 mV. Symmetrical Pt electrodes (Demetron 308A) were applied on both sides of the pellets, which were then fired at 1100 °C for 30 min. The impedance measurements were performed in air over a temperature range of 100–800 °C with 25 °C steps and in a reductive atmosphere (Ar/4% H_2) between 400 and 600 °C at 50 °C steps.

Electrochemical performance was measured by impedance spectroscopy with a symmetric cell configuration using frequency response analyser (Solartron 1260) in the frequency range of 13 MHz to 0.05 Hz, with AC current amplitude of 50 mA, in air and under reducing atmosphere (Ar/4% H_2) at 600 °C. The symmetric cells consisted of 8 mol% yttria-stabilised zirconia (YSZ) (TZ-8YS Tosoh) electrolytes with platinum or LSAM as electrodes in order to evaluate the performance of LSAM by comparison. YSZ powder was formed into pellets by uniaxial pressing (100 MPa) followed by isostatic pressing (200 MPa), and sintered with heating rate of 5 °C/min up to 1500 °C with dwell time of 4 h and cooling rates of 5 °C/min to room temperature. A commercial platinum paste (Demetron 308A) and a paste produced by mixing LSAM powder with a terpineol-based ink vehicle (Fuel Cell Materials) were applied onto both sides of the YSZ pellets by brushing and then sintered in air at 1100 °C for 30 min and 1.5 h, respectively. All impedance spectra were analysed with ZView® software (Scribner Associates, Inc.).

III. Results and discussion

3.1. Density, crystalline phases and microstructure

Figure 1 presents the X-ray diffractograms of the sintered samples. The diffraction peaks are indexed to the cubic perovskite structure of $LaAlO_3$ (JCPDS card 85-848), with La_2O_3 (JCPDS: 73-2141) detected as a residual secondary phase in all samples. Rietveld refinement results show that the amount of La_2O_3 is less than 5 wt.% in all samples but the LSA ones sintered at 1600 °C, as indicated by the very low intensities of the peaks indexed for this phase. The exception presented by the LSA samples sintered at 1600 °C will be clarified later along the discussion concerning the microstructural results. Besides, the presence of La_2O_3 as residual phase after sintering at high temperatures ($T \geq 1500$ °C) indicates that the ratio of compounds in the starting raw materials was higher in La_2O_3. This left the composition of the sintered samples in the La_2O_3-$LaAlO_3$ field, which is slightly to the left of the $LaAlO_3$ line composition in the phase equilibria diagram of the La_2O_3-Al_2O_3 system [12].

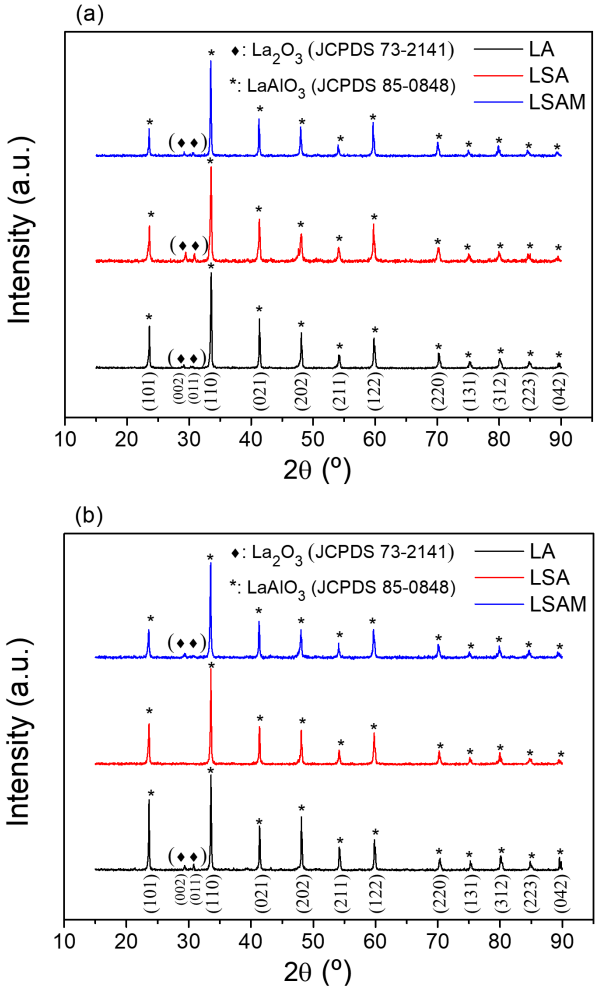

Figure 1. X-ray diffractograms of LA, LSA and LSAM samples sintered at 1500 °C (a) and 1600 °C (b) for 6 h

Table 2 presents the lattice parameters, evaluated from XRD data, and the theoretical density, which was calculated using following equation:

$$\rho_{theo} = \frac{\sum A}{V \cdot N_A} \quad (1)$$

where $\sum A$ is the sum of the atomic weights of all the atoms in the unit cell, N_A is the Avogadro number (6.023×10^{23} mol^{-1}) and V is the unit cell volume. The unit cell parameters were determined by a Rietveld refinement of the X-ray diffraction pattern and considering 0.1 oxygen deficiency relative to oxygen sites for LSA. Table 2 also exhibits the percentage of relative density of the samples sintered at 1500 and 1600 °C.

The weight of each ion per unit cell is given by:

$$\rho_{ion} = \frac{N_s \cdot O_s \cdot A_A}{N_A} \quad (2)$$

where N_s is number of sites, O_s is fraction of occupied sites and A_A is atomic weight [2]. Each unit cell of $LaAlO_3$ has one La^{3+} cation, one Al^{3+} cation and three O^{2-} anions, so:

$$\sum A = 1 \cdot A_{La} + 1 \cdot A_{Al} + 3 \cdot A_O \quad (3)$$

where A_{La} is the La^{3+} atomic weight, A_{Al} is the Al^{3+} atomic weight and A_O is the O^{2-} atomic weight. When doped the chemical formula becomes $(La_{1-x}M_x)Al_{1-y}N_y)O_{3-\delta}$, therefore:

$$\sum A = [(1-x)A_{La} + xA_M] + [(1-y)A_{Al} + yA_N] + (3-\delta)A_O \quad (4)$$

where x and A_M are the amount and atomic weight of the La^{3+} site dopant, respectively, and y and A_N are the amount and atomic weight of the Al^{3+} site dopant, respectively.

Theoretically, Sr^{2+} cations occupy the same positions as La^{3+} when added to the $LaAlO_3$ perovskite structure, which leads to a decrease of the theoretical density, as shown in Table 2, due to the lower atomic weight of Sr^{2+} (87.62 g/mol) compared to La^{3+} (138.9055 g/mol). In contrast, Mn co-doped samples present a lesser decrease in theoretical density, since Mn occupies the same position as Al, and Mn atomic weight (54.938 g/mol) is higher than Al (26.981 g/mol), compensating some of the difference between Sr^{2+} and La^{3+}.

The substitution of La for Sr may also be responsible for the lower theoretical density due to the creation of oxygen vacancies in order to maintain charge neutrality in the structure. Oxygen vacancies are generated to compensate the charge of the substitution of Sr^{2+} ions in the La-cation sublattice, according to defect reaction (Eq. 5) where notation of defects by Kroger and Vink was adopted [13]:

$$2\,SrO \xrightarrow{LaAlO_3} La_{La} + 2\,Sr'_{La} + Al_{Al} + 2\,O_O + V_O^{\bullet\bullet} \quad (5)$$

In these compositions, the concentration of oxygen vacancy per unit cell (δ) is 0.1, since $[V_O^{\bullet\bullet}] = \delta$.

For the Al site doping (LSAM), if considering Mn valence being the same as Al, its presence in the crystalline lattice does not introduce additional oxygen vacancies. However, for relatively high oxygen pressures

Table 2. Lattice parameter and theoretical and relative densities of sintered samples

Composition	Lattice parameter [Å]		Theoretical density [g/cm^3]	Relative density [%TD]	
	1500 °C	1600 °C		1500 °C	1600 °C
LA	3.7915(1)	3.7914(1)	6.52	99.2	99.9
LSA	3.7986(3)	3.7970(2)	6.13	96.6	97.3
LSAM	3.8006(3)	3.8011(3)	6.32	91.4	98.2

(p_{O_2} ~ 1–0.01 atm), the oxygen vacancies [$V_O^{\bullet\bullet}$] created by the introduction of an aliovalent cation in La site, such as Sr, is mainly compensated electronically by the oxidation of Mn^{3+} ions to Mn^{4+} ions [9,10]. A significant amount of ionic compensation by double-positively charged oxygen vacancies is unlikely due to the presence of Mn, as indicated by Eq. 6:

$$2\,Mn_{Al}^{x} + V_O^{\bullet\bullet} + \frac{1}{2}\,O_2 \longrightarrow 2\,Mn_{Al}^{\bullet} + O_O^{x} \qquad (6)$$

Thus, under oxidant atmosphere, the amount of oxygen vacancies in the lattice is very small. Therefore, to calculate the theoretical density, the value of δ was considered to be approximately equal to zero. The chemical formula for this composition is $La_{0.8}Sr_{0.2}Al_{0.8}Mn_{0.2}O_3$.

The observed increase in cell parameters of the Sr and Sr-Mn co-doped samples (Table 2) indicates the successful formation of solid solution, which can be attributed to the substitution of La^{3+} by Sr^{2+} ions in the A site and Al^{3+} to Mn_3^{+} ions in the B site, considering that the ionic radii for La^{3+} is 1.36 Å, for Sr^{2+} is 1.44 Å, for Al^{3+} is 0.535 Å and for Mn^{3+} is 0.58 Å [14].

Figures 2, 3 and 4 depict the microstructures of the polished and etched surfaces of the sintered samples along with calculated grain size distribution. The BSE images of the undoped $LaAlO_3$ and Sr-Mn co-doped samples (Figs. 2 and 3) show homogeneous microstructure, while the Sr-doped samples (Fig. 4) present a chemically heterogeneous microstructure composed of bright and dark grains. Since BSE images provide con-

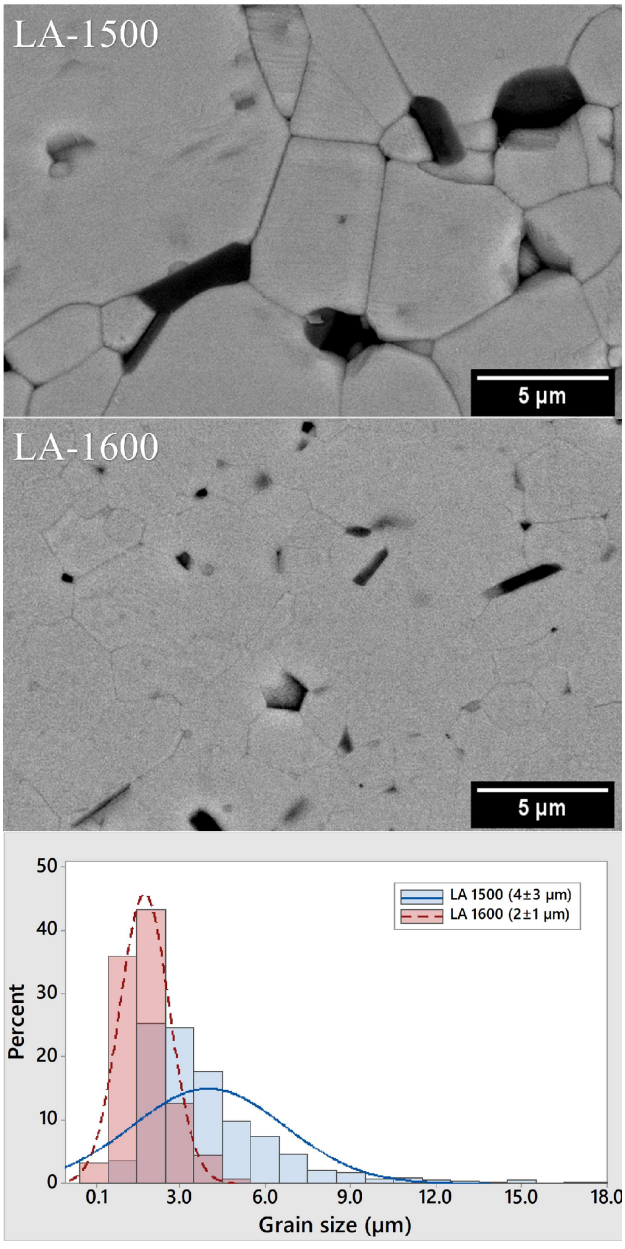

Figure 2. SEM micrographs of polished and etched surfaces, and calculated grain size distribution of LA samples sintered at 1500 and 1600 °C

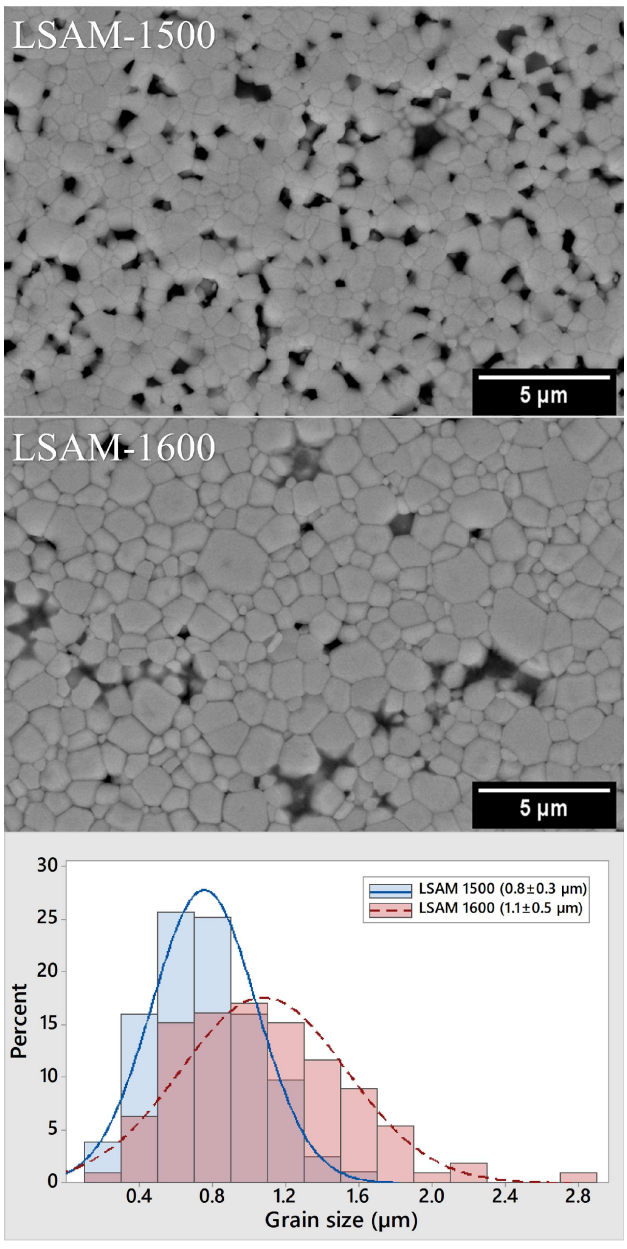

Figure 3. SEM micrographs of polished and etched surfaces, and calculated grain size distribution of LSAM samples sintered at 1500 and 1600 °C

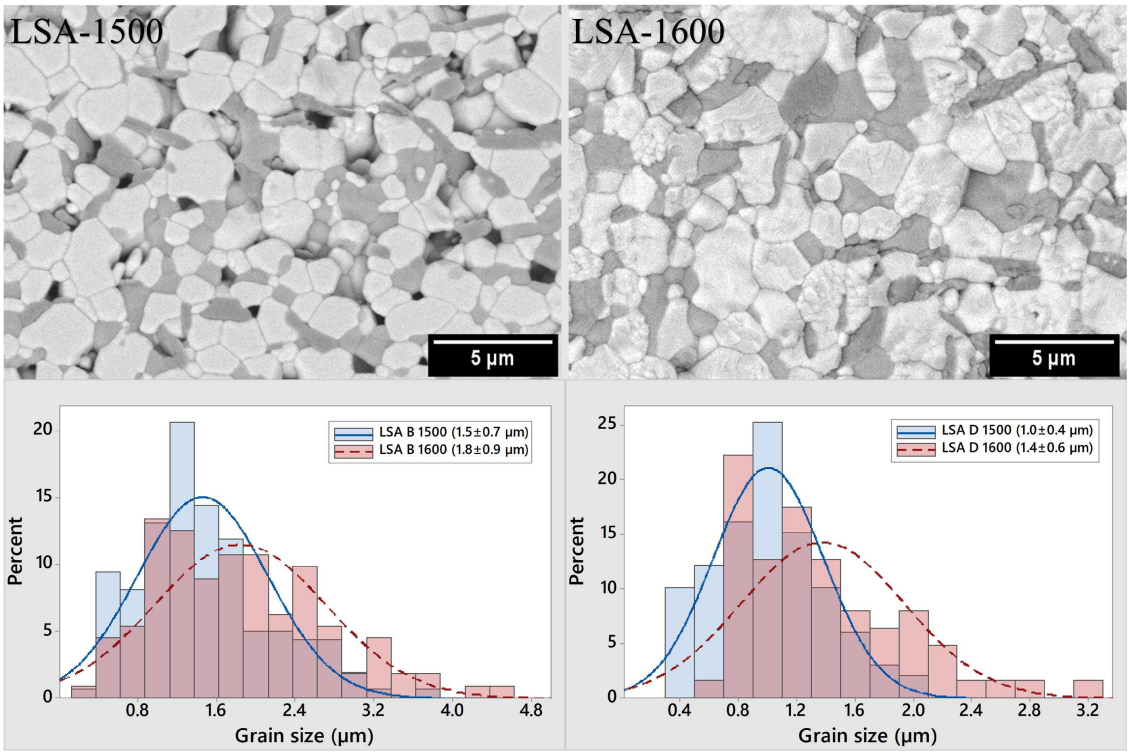

Figure 4. SEM micrographs of polished and etched surfaces, and calculated grain size distribution for bright and dark grains of LSA samples sintered at 1500 and 1600 °C

trast due to atomic number differences, i.e. larger atoms scatter more electrons compared to lighter ones and thus create a higher signal, the dark regions correspond to a phase rich in low atomic number elements as compared to the brighter matrix. The brighter grains are richer in La, while the darker grains have a composition closer to that of the theoretical phase, in similar way to other published results [3,15].

It is also interesting to note the differences in grain size and grain size distribution of the different compositions and sintering conditions. Despite the compositional homogeneity mentioned earlier in the undoped compositions (Fig. 2), the samples sintered at 1500 °C present larger grains and broader size distribution than samples sintered at 1600 °C. Calcination in the temperature range of 700–1000 °C is sufficient to crystallize the $LaAlO_3$ perovskite structure in the starting powders, which were obtained by chemical routes, with the crystallite size increasing directly proportional to the calcination temperature [16,17]. However, the solid-state reaction route leads to larger crystallite sizes when compared to chemical synthesis routes [17,18]. In this way, the powders obtained by solid-state reaction after the successive steps of calcination, as described in Section 2, are crystallized in the desired crystal structure of $LaAlO_3$, however, the crystallites may present a heterogeneous size distribution. Therefore, the heating rate of 10 °C/min up to 1600 °C may offer enough thermal energy in a shorter period of time to homogenize the crystallite sizes and to densify the samples during the sintering process, leading the samples to reach the grain growth regime with a well-established perovskite structure that is refractory. This may explain the smaller average grain size and narrower size distribution. Conversely, at 1500 °C, there may not be enough thermal energy in the same window of time, resulting in a heterogeneous development of microstructure, similar to an abnormal grain growth process [19], which in turn may explain the larger average grain size and broader size distribution.

On the other hand, the addition of dopants (Sr and Mn) may lower the energy barrier and facilitate the kinetics of crystallization for the perovskite structure during the sintering process at an earlier moment than the undoped samples, so that the LSAM (Fig. 3) and LSA (Fig. 4) samples present smaller average grain sizes than the undoped ones (Fig. 2), as well as a traditional trend of increase of grain size as function of temperature. However, average grain sizes are larger and size distributions are broader for LSA than LSAM samples, indicating that the formation of charge compensating defects that enhance mass transport during sintering [20] is higher in the presence of Sr alone than the combination of Sr and Mn, as discussed previously (Eqs. 4 and 5). This higher mobility caused by the Sr doping could also facilitate the incorporation of the residual La_2O_3 into the $LaAlO_3$ structure at the higher sintering temperature (1600 °C). Accordingly, this explains the lack of peaks for the La_2O_3 phase in the X-ray diffractogram of LSA samples sintered at 1600 °C (Fig. 1b) as well as the development of the chemically heterogeneous microstructure observed in LSA samples (Fig. 4), with some grains richer in La as discussed previously. The distribution of Sr is uniform and homogeneous throughout the en-

tire sample, as shown by EDS analysis in a previous work [15].

3.2. Electrical conductivity

The LA, LSA and LSAM sintered samples were analysed by impedance spectroscopy in air at temperatures between 100 and 800 °C at 25 °C intervals. Figure 5 shows the impedance spectra of the LA, LSA and LSAM samples corrected for their thickness and electrode area. The LA samples are highly resistive and present only the beginning of one semicircle. In the pure $LaAlO_3$, the ionic conduction occurs by the movement of oxygen ion carriers through oxygen vacancies. It is very low since the formation of intrinsic oxygen vacancies through the thermally activated process is difficult due to the high binding strength of Al–O [21]. Thus, the pure $LaAlO_3$ exhibits low ionic conductivity and consequently high activation energy, since the activation energies for non-doped samples have to include the enthalpy for formation of oxygen vacancies as well as the enthalpy for the migration of these ions. For the LSA and LSAM samples, the Nyquist plots are typical and exhibit two semicircles: the high frequency one is attributed to the bulk response and the low frequency one to the grain boundary. For the LSA samples, the resistance related to the grain boundary semicircle is higher than the resistance of the bulk semicircle, but for the LSAM samples, they have similar resistances. As the temperature increases, the higher frequency semicircle gradually disappears, for the LSA this temperature is at 500 °C, while for the LSAM it is 200 °C.

The impedance spectra were analysed through data fitting, using the ZView program and equivalent elementary circuits arranged in series consisting of one resistance (R) and one constant phase element (CPE) in parallel. Figure 6 depicts the Arrhenius plots of total electrical conductivities measured in air for the LA, LSA and LSAM samples sintered at 1500 and 1600 °C/6 h. The total electrical conductivity increases with Sr doping (5.74×10^{-4} S/cm at 600 °C) compared to LA (2.96×10^{-6} S/cm at 600 °C) for samples sintered at 1600 °C. Equation 5 shows that the number of oxygen vacancies can be increased by replacing La^{3+} with smaller valence cations, such as Sr^{2+} and Ca^{2+}, at the A site. It also can be increased by replacing Al^{3+} with smaller valence cations, such as Mg^{2+}, at the B site, or by both substitu-

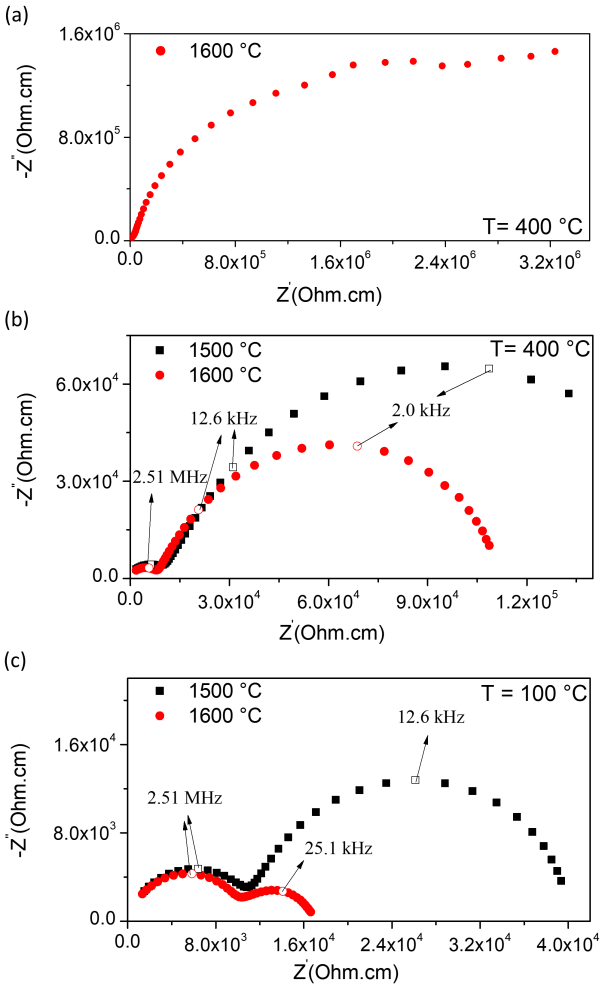

Figure 5. Impedance spectroscopy spectra, measured in air for LA (a), LSA (b) and LSAM (c) samples sintered at 1500 and 1600 °C/6 h

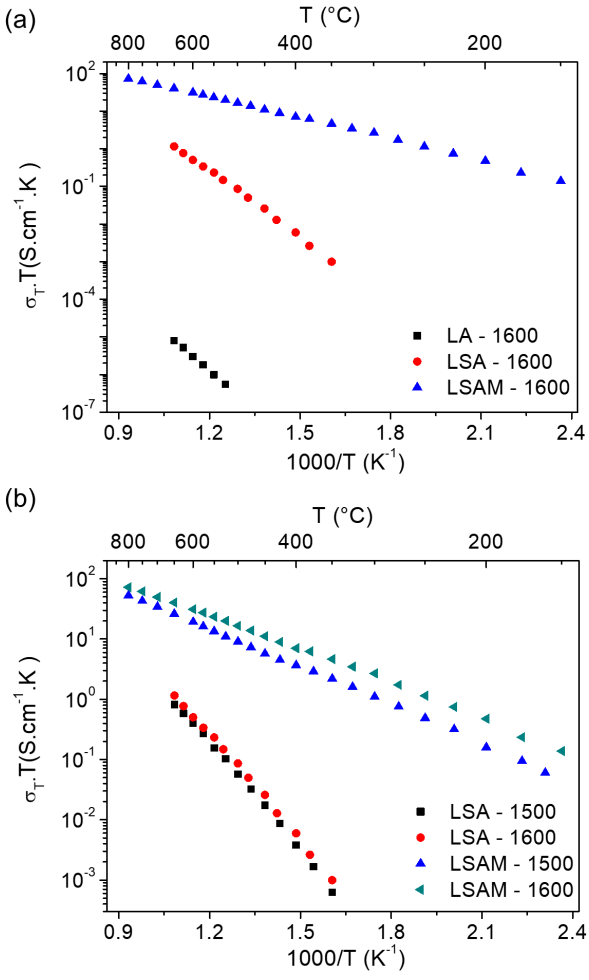

Figure 6. Arrhenius plots of total electrical conductivity measured in air for: LA, LSA and LSAM samples sintered at 1600 °C/6 h (a) and LSA and LSAM samples sintered at 1500 and 1600 °C/6 h (b)

Table 3. Comparison of total electrical conductivity (σ_T) at 800 °C in air and activation energy (E_a)

Composition	σ_T [S/cm] at 800 °C		E_a [eV]	
	1500 °C/6 h	1600 °C/6 h	1500 °C/6 h	1600 °C/6 h
LSA	1.0×10^{-3}	8.9×10^{-3}	1.18 ± 0.01	1.16 ± 0.02
LSAM	4.9×10^{-2}	6.8×10^{-2}	0.411 ± 0.002	0.359 ± 0.002

tions at A and B sites. Consequently, ionic conduction is significantly enhanced, in this case, by three orders of magnitude by Sr addition. With Mn co-doping, the total electrical conductivity increased by five and two orders of magnitude (3.6×10^{-2} S/cm at 600 °C) compared with the LA and LSA samples, respectively. The Mn co-doped samples exhibit higher electrical conductivity and lower activation energy, which may be due to an electronic conduction.

Table 3 presents the total electrical conductivity (σ_T) at 800 °C and the activation energies (E_a), which were calculated by linear fitting of the data presented in Fig. 6, for the LSA and LSAM samples.

It is well established in the literature that doped $LaAlO_3$ is a p-type electronic conductor under oxidizing conditions. The defect equilibria, based on the oxygen vacancies generated by dopants (Sr, Mg) and filled by oxygen gas at high oxygen partial pressure (p_{O_2}), can be used to explain the observed conductivity behaviour. This suggests the appearance of hole conduction in perovskite oxides according to [22]:

$$\frac{1}{2}\,O_2(g) + V_O^{\bullet\bullet} \longrightarrow O_O^x + 2\,h^{\bullet} \qquad (7)$$

where $[V_O^{\bullet\bullet}]$ is the oxygen vacancy, O_O^x the oxygen ion at normal lattice site, $h^{\bullet}$ electronic hole.

To understand the p-type semiconductor behaviour of $LaAlO_3$, the LSA samples were co-doped with Mn, since Mn ions can have different valences at high temperatures during sintering. In order to better evaluate the higher conductivity of the Mn co-doped sample, the LSA and LSAM were submitted to the conductivity measurement in reducing atmosphere. Figure 7 compares the total electrical conductivity measured in low oxygen partial pressure (Ar/H_2) with those in air for the LSA and LSAM samples sintered at 1600 °C/6 h.

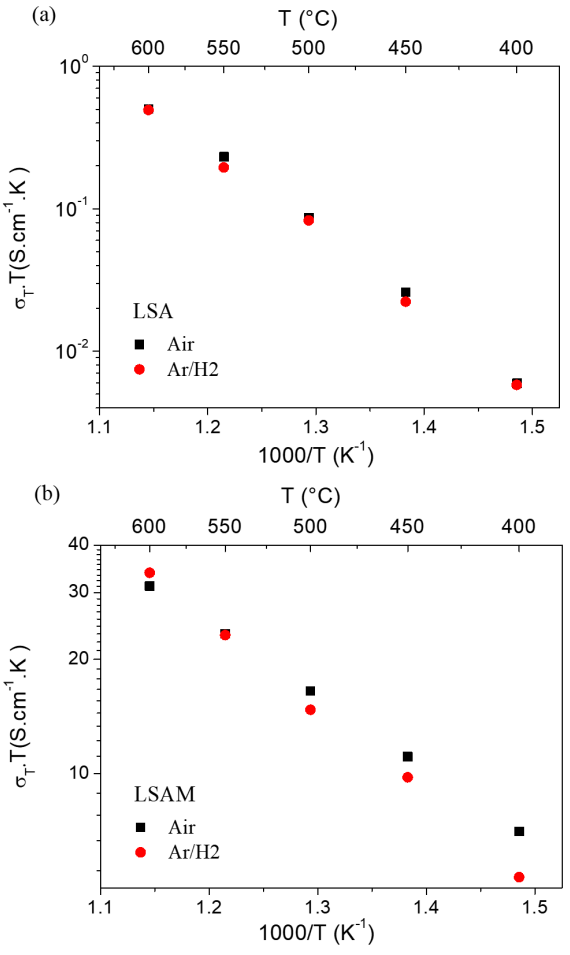

Figure 7. Arrhenius plots of total electrical conductivity measured in low oxygen partial pressure and in air for LSA (a) and LSAM (b) samples sintered at 1600 °C/6 h

Table 4. Comparison of activation energy (E_a) in air and under low oxygen partial pressures (Ar/4% H_2)

Composition	E_a [eV]	
	1500 °C/6 h	1600 °C/6 h
LSA	1.16 ± 0.02	1.13 ± 0.03
LSAM	0.359 ± 0.002	0.46 ± 0.01

Table 4 presents activation energies (E_a) calculated by linear fitting of the data presented in Fig. 7 for the LSA and LSAM samples in reducing atmosphere (Ar/4% H_2) and in air. Conductivity of the LSA samples shows no dependence with the type of atmosphere, so conductivity and activation energies are the same for reducing and oxidant atmospheres. Meanwhile, the LSAM samples exhibit lower conductivity and higher activation energy in Ar/4% H_2 than in air, which suggests the appearance of relatively large p-type semiconductor behaviour under high oxygen partial pressures. The high electronic conductivity presented by the Mn co-doped composition can be attributed to the mechanism of small polaron hopping due to the presence of Mn^{3+} and Mn^{4+} ions [9]:

$$2\,Mn_{Al}^x + V_O^{\bullet\bullet} + \frac{1}{2}\,O_2 \longrightarrow 2\,Mn_{Mn}^{\bullet} + O_O^x \qquad (8)$$

The LSAM exhibits higher electrical conductivity than the LSA sample both in air and reducing atmosphere, indicating that LSA is mainly an oxide ionic conductor, while LSAM is dominated by p-type electronic conduction. Table 5 compares total electrical conductivity data reported in the literature of samples with

Table 5. Total electrical conductivity for LSA and LSAM sintered at 1600 °C/6 h compared to values reported in the literature

Composition	Measured temperature [°C]	Measured atmosphere	σ_T [S/cm]	Reference
$La_{0.8}Sr_{0.2}AlO_{3-\delta}$	800	Air	8.9×10^{-3}	this work
$La_{0.8}Sr_{0.2}AlO_{3-\delta}$	800	Ar/H_2	7.7×10^{-3}	this work
$La_{0.8}Sr_{0.2}Al_{0.8}Mn_{0.2}O_{3-\delta}$	800	Air	6.8×10^{-2}	this work
$La_{0.8}Sr_{0.2}Al_{0.8}Mn_{0.2}O_{3-\delta}$	800	Ar/H_2	0.11	this work
$LaAlO_3$	800	Air	2.0×10^{-3}	[21]
$La_{0.9}Sr_{0.1}AlO_{3-\delta}$	800	Air	2.0×10^{-3}	[22]
$La_{0.8}Sr_{0.2}AlO_{3-\delta}$	800	Air	5.0×10^{-3}	[21]
$La_{0.8}Sr_{0.2}Al_{0.7}Mn_{0.3}O_{3-\delta}$	810	Air	0.74	[10]
$La_{0.8}Sr_{0.2}Al_{0.5}Mn_{0.5}O_{3-\delta}$	810	Air	10	[10]
$La_{0.8}Sr_{0.2}Al_{0.5}Mn_{0.5}O_{3-\delta}$	810	Ar/H_2	2.7	[10]
$La_{0.8}Sr_{0.2}Al_{0.5}Mn_{0.5}O_{3-\delta}$	800	Air	8.6 ± 0.3	[7]

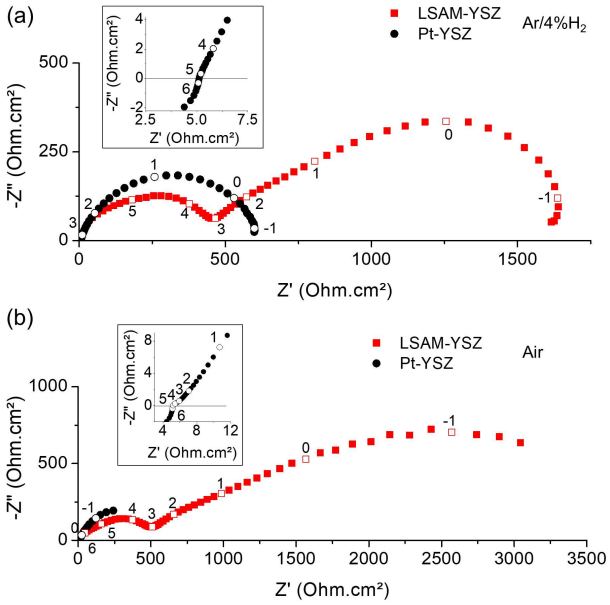

Figure 8. Impedance spectra of one electrode for LSAM-YSZ and Pt-YSZ showing electrode polarization resistances in Ar/4% H_2 (a) and air (b) at 600 °C (insets present a magnified view of the high frequency region of Pt-YSZ electrodes and open symbols indicate the frequency decades)

similar chemical compositions used in this work with the results of LSA and LSAM in different atmospheres. It is interesting to note that LSAM with only 20 mol% of Mn presents total conductivities close to that of compounds with higher concentrations of Mn (30 and 50 mol%).

Figure 8 presents the impedance spectra of one electrode for LSAM-YSZ-LSAM and Pt-YSZ-Pt symmetric cells. The polarization resistance of the symmetric cell was divided by two to obtain the contribution from one single electrode and normalized by the area. The differences in the frequency range of electrode response in air and Ar/4% H_2 of Pt electrodes indicate that oxygen oxidation reaction is slower than the hydrogen reduction reaction and requires more energy to happen (higher polarization resistance).

The high total polarization resistance of the samples can be attributed to the small number of triple phase boundary (TPB) points, considering that electrode microstructures were not optimized by grading or deposition method. However, the comparison with Pt shows that LSAM presents catalytic activity for electrode reactions even with a low dopant concentration.

IV. Conclusions

$LaAlO_3$ (LA), $La_{0.8}Sr_{0.2}AlO_{3-\delta}$ (LSA) and $La_{0.8}Sr_{0.2}Al_{0.8}Mn_{0.2}O_{3-\delta}$ (LSAM) perovskite ceramics were successfully obtained by solid state reaction and sintering at 1500 and 1600 °C. Sr and Mn additions played an important role in the stabilization of the perovskite structure, which affected chemical homogeneity and grain growth. The LA and LSAM ceramics showed homogeneous microstructure, while the LSA samples presented grains with slightly different compositions: grains rich in Al and deficient in La, and grains with a composition closer to that of the theoretical phase.

The LSAM samples presented mixed electrical conductivity, combining ionic with p-type electronic conductivity, which lead to an increase in total electrical conductivity of five and two orders of magnitude compared to the LA and LSA samples, respectively, which are oxide ionic conductors. The electrical conductivity of the LSAM reached 0.11 S/cm at 800 °C under typical SOFC anode conditions, and the LSAM also presents catalytic activity for electrode reactions even with a low dopant concentration (20 mol%).

Acknowledgement: The authors gratefully acknowledge the financial support of CNPq and Capes - Brazil and the technical support of LCE (Structural Characterization Laboratory) - DEMa/UFSCar - Brazil.

References

1. V.N. Stathopoulos, T. Kuznetsova, O. Lapina, D. Khabibulin, P.K. Pandis, T. Krieger, Y. Chesalov, R. Gulyalev, V. Krivensov, T. Larina, V. Sadykov, "Evolution of bulk and surface structures in stoichiometric $LaAlO_3$ mixed oxide prepared by using starch as template", *Mater. Chem. Phys.*, **207** (2018) 423–434.
2. O.N. Verma, N.K. Singh, Raghvendra, P. Singh, "Study

of ion dynamics in lanthanum aluminate probed by conductivity spectroscopy", *RSC Advances*, **5** (2015) 21614–21619.
3. P.S. Anderson, G.C. Mather, F.M.B. Marques, D.C. Sinclair, A.R. West, "Synthesis and characterisation of $La_{0.95}Sr_{0.05}GaO_{3-\delta}$, $La_{0.95}Sr_{0.05}AlO_{3-\delta}$ and $Y_{0.95}Sr_{0.05}AlO_{3-\delta}$", *J. Eur. Ceram. Soc.*, **19** (1999) 1665–1673.
4. H. Zhu, P. Zhang, S. Dai, "Recent advances of lanthanum-based perovskite oxides for catalysis", *ACS Catalysis*, **5** (2015) 6370–6385.
5. N. Das, S. Kandimalla, "Application of perovskites towards remediation of environmental pollutants: an overview", *Int. J. Environm. Sci. Technol.*, **14** (2017) 1559–1572.
6. G. Qin, X. Huang, J. Chen, Z. He, "Synthesis of Sr and Mg double-doped $LaAlO_3$ nanopowders via EDTA-glycine combined process", *Powder Technol.*, **235** (2013) 880–885.
7. C.A. da Silva, P.E.V. de Miranda, "Synthesis of $LaAlO_3$ based materials for potential use as methane-fueled solid oxide fuel cell anodes", *Int. J. Hydrogen Energy*, **40** (2015) 10002–10015.
8. T.-Y. Chen, R.-Y. Pan, K.-Z. Fung, "Effect of divalent dopants on crystal structure and electrical properties of $LaAlO_3$ perovskite", *J. Phys. Chem. Solids*, **69** (2008) 540–546.
9. Q.X. Fu, F. Tietz, P. Lersch, D. Stöver, "Evaluation of Sr- and Mn-substituted $LaAlO_3$ as potential SOFC anode materials", *Solid State Ionics*, **177** (2006) 1059–1069.
10. Q. Fu, F. Tietz, D. Stöver, "Synthesis and electrical conductivity of Sr- and Mn-substituted $LaAlO_3$ as a possible SOFC anode material", *Solid State Ionics*, **177** (2006) 1819–1822.
11. T.-Y. Chen, K.-Z. Fung, "A and B-site substitution of the solid electrolyte $LaGaO_3$ and $LaAlO_3$ with the alkaline-earth oxides MgO and SrO", *J. Alloys Compds.*, **368** (2004) 106–115.
12. I.A. Bondar', N.V. Vinogradova, "Phase equilibria in the lanthanum oxide - alumina system", *Bull. Academy Sci. USSR Div. Chem. Sci.*, **13** (1964) 737–741.
13. F.A. Kröger, H.J. Vink, "Relations between the concentrations of imperfections in solids", *J. Phys. Chem. Solids*, **5** (1958) 208–223.
14. R. Shannon, "Revised effective ionic radii and systematic studies of interatomic distances in halides and chalcogenides", *Acta Crystallogr. A*, **32** (1976) 751–767.
15. L.A. Villas-Boas, D.P.F.d. Souza, "The effect of Pr co-doping on the densification and electrical properties of Sr-$LaAlO_3$", *Mater. Res.*, **16** (2013) 982–989.
16. E. Taspinar, A.C. Tas, "Low-temperature chemical synthesis of lanthanum monoaluminate", *J. Am. Ceram. Soc.*, **80** (1997) 133–141.
17. L. Djoudi, M. Omari, N. Madoui, "Synthesis and characterization of lanthanum monoaluminate by co-precipitation method", *EPJ Web Conferences*, **29** (2012) 00016.
18. W. Haron, A. Wisitsoraat, S. Wongnawa, "Comparison of nanocrystalline $LaMO_3$ (M = Co, Al) perovskite oxide prepared by co-precipitation method", *Int. J. Chem. Eng. Appl.*, **5** (2014) 123–126.
19. M.N. Rahaman, *Sintering of Ceramics*, CRC Press, 2007.
20. S. Nikodemski, J. Tong, R. O'Hayre, "Solid-state reactive sintering mechanism for proton conducting ceramics", *Solid State Ionics*, **253** (2013) 201–210.
21. T.-Y. Chen, K.-Z. Fung, "Comparison of dissolution behavior and ionic conduction between Sr and/or Mg doped $LaGaO_3$ and $LaAlO_3$", *J. Power Sources*, **132** (2004) 1–10.
22. K. Nomura, S. Tanase, "Electrical conduction behavior in $(La_{0.9}Sr_{0.1})M^{III}O_{3-\delta}$ (M^{III} = Al, Ga, Sc, In, and Lu) perovskites", *Solid State Ionics*, **98** (1997) 229–236.